PAPER

Check for updates

Quantification of laser-induced aerosols by microdroplet calibration and investigation of matrix effects using LA-ICP-TOFMS†

Tobias Schöberl, [ID] Mirjam Bachmann and Detlef Günther [ID] *

The application of monodisperse microdroplets for non-matrix-matched quantification in LA-ICP-TOFMS was investigated for inorganic and organic matrices. Suppression behavior in droplet signals caused by addition of typical major elements of geological samples (Al, Si, Ca, Ti, and Fe) in the $\mu g\ g^{-1}$ range was studied using microdroplets introduced *via* a falling tube and compared to solution nebulization. Signal suppression patterns observed for microdroplets could be attributed to neither mass load effects nor in-plasma oxide formation, nor reproduced *via* solution nebulization, suggesting a fundamentally different behavior of microdroplets in the plasma. Radial diffusion profiles were acquired to assess in-plasma behavior of droplets and laser-induced aerosol from NIST SRM 610 (glass). Diffusion profiles overlapped and showed similar full width at half maxima (FWHM) for microdroplets and the laser-induced aerosol, with minor spatial shifts in intensity maxima, likely due to not complete on-axis droplet introduction into the plasma. Quantification based on microdroplet calibration yielded relative deviations from reference values below ±20% across certified reference materials and an in-house prepared gelatine standard. Quantification of gelatine samples using NIST SRM 610 (glass) as an external standard resulted in larger deviations compared to droplet-based calibration, which yielded values in agreement with digestion data. These results demonstrate the suitability of monodisperse microdroplets for non-matrix-matched calibration in LA-ICP-TOFMS, particularly for elements non-certified or uncommonly reported in reference materials used in LA-ICP-MS.

Introduction

Since its introduction 40 years ago,[1] laser ablation inductively coupled plasma mass spectrometry (LA-ICP-MS) has become a widely applied analytical technique for multi-elemental analysis for major, minor and trace components, achieving detection limits in the fg to ag range.[2] Although LA-ICP-MS enables rapid analysis of a wide variety of solid samples with minimal material consumption, quantification can remain challenging due to matrix-dependent laser-sample interactions.[3] To address this, several strategies have been developed over the years. Matrix-matched quantification using certified reference materials (CRMs) or in-house prepared standards remains the most commonly employed approach.[4-7] Alternatively, non-matrix-matched quantification using liquid calibration standards was pioneered by Thompson *et al.* using ICP-atomic emission spectrometry (ICP-AES),[8] followed by Cromwell *et al.* for ICP-MS.[9] Despite agreeing with literature values (±25% deviation from reference values), Cromwell *et al.* reported that the high

solvent load introduced by solution nebulization led to increased oxide formation resulting in reduced sensitivity and polyatomic interferences. To mitigate oxide formation, subsequent efforts focused on reducing solvent load by direct ablation of liquids (±10% deviation from reference values)[10] or desolvation systems (±25% deviation from reference values).[11,12] However, elemental losses during desolvation impeded accurate quantification of, *e.g.*, Cu, as reported by Halicz *et al.*[12] Such elemental losses by desolvation have also been reported for elements such as Ga, Ge, Zn,[13] Mo[14] and B[15]. Alternative strategies for the quantification of solids with liquids include ablation of micro dried droplets,[16] ablation from self-aliquoting micro-grooves[17] or laser ablation of solids in liquids (LASIL).[18,19] More recently, Mervič *et al.*[20,21] demonstrated a non-matrix-matched calibration approach based on ablation volume normalization by characterizing the sample surface morphology well before and after ablation using optical profilometry, applied successfully across diverse materials. Most of these approaches employ solution nebulization to introduce the liquid calibrant, producing a polydisperse aerosol that is transported into the ICP. An alternative approach involves the use of monodisperse microdroplets, which have been used as a tool for investigation of fundamental flame[22] and plasma[23] processes and gained renewed interest in the past 15

Laboratory of Inorganic Chemistry, Department of Chemistry and Applied Biosciences, ETH Zurich, 8093 Zurich, Switzerland

† Electronic supplementary information (ESI) available. See DOI: https://doi.org/10.1039/d5ja00171d

years for applications in single-particle ICP-MS (sp-ICP-MS).[24–29] Microdroplets can be introduced discretely into the ICP *via* a falling tube[24] using He/Ar as drying and transport gases[30] and are detected using either SFMS, QMS or TOFMS technology. Upon drying, the dissolved salts crystallize to form a nanoparticle-like salt residue,[28] which is expected to exhibit in-plasma behavior similar to that of nanoparticles and agglomerates generated by laser ablation.[31] Borovinskaya[32] demonstrated this concept on NIST SRM 610 (glass), reporting deviations of ±20% from certified values, highlighting the potential of this approach for non-matrix-matched quantification.

This work investigates the suitability of monodisperse microdroplets for non-matrix-matched quantification in LA-ICP-TOFMS across different sample matrices and a wide range of elements. Matrix-induced suppression of analyte signals in droplets was studied and compared to conventional solution nebulization (SN). In addition, in-plasma behavior of micro-droplets and laser-induced aerosols was compared by using radial diffusion profiles of various analytes. Finally, the obtained quantification results will be discussed.

Experimental

Instrumentation

All measurements were carried out using an ArF* 193 nm excimer laser system (GeoLas C, Lambda Physik, Germany) with an implemented modified parallel flow ablation cell (MPFAC), as described elsewhere.[33] The MPFAC was operated with a carrier gas mixture of He (0.65 to 0.8 L min⁻¹) and Ar (0.55 to 0.75 L min⁻¹) and connected to an adapted dual sample introduction setup,[25] allowing for the combined introduction of laser-induced aerosols and microdroplets. Aerosols were introduced into an ICP time of flight (TOF) mass spectrometer (icpTOF2R, TOFWERK AG, Switzerland), enabling quasi-simultaneous detection over a mass range of $m/z = 14$ to 254.[34] The instrument was tuned daily to ensure high sensitivity, a $^{232}\mathrm{Th}^{16}\mathrm{O}^+/^{232}\mathrm{Th}^+$ formation rate below 1%, a $^{238}\mathrm{U}^+/^{232}\mathrm{Th}^+$ ratio of 0.9 to 1.1 and expected isotope abundance patterns for the rare earth elements (REEs). Background correction was performed using gas blanks for LA measurements and an acidified blank solution with Cs as the tracer for microdroplet measurements.

Monodisperse microdroplets were generated using an Autodrop Pipette (AD-KH-501-L6) with a nominal nozzle size of 50 μm and an external control unit (microdrop technologies, Germany). The resulting droplets ranged in diameter from 60–75 μm. Droplets were focused into the falling tube, and dried and transported using a He flow (0.4 to 0.75 L min⁻¹) before being merged with the LA carrier gas flow *via* a T-piece. No active heating was applied during droplet transport.

For quantification of gelatine digests, the samples were measured employing ICP-optical emission spectrometry (ICP-OES) using a radial spectrometer (Arcos, Spectro Analytical Instruments, Germany) in Paschen-Runge geometry. The instrument was connected to a Scott-type spray chamber equipped with a crossflow nebulizer (Ar flow: 1 L min⁻¹). The

instrument was tuned for maximum sensitivity, with an Ar(I) 404.442 nm intensity of 800 kcps to 1500 kcps and a Mg(II) 280.271 nm/Mg(I) 285.213 nm ratio of >9.5.[35]

All specific operating conditions used in this study are summarized in the ESI in Table S2.†

Liquid sample preparation

All vials used were conditioned in 10% sub-boiled HNO₃ (v/v) (p.a. > 65%, Sigma-Aldrich, Germany) and 10% HCl (v/v) (p.a. > 37%, Fisher Scientific, Germany) and stored under 1% sub-boiled HNO₃. Liquid calibration standards were prepared from single- and multi-element stock solutions (Inorganic Ventures, USA; Merck, Germany) and stabilized in diluted sub-boiled HNO₃ and HCl prepared in ultrapure water (18.2 MΩ cm, Millipore, USA). All solutions were prepared gravimetrically with an accuracy of 0.1 mg (Mettler Toledo, Germany). For parameter studies, analytes were limited to Sr, Rh, In, the REEs (Sc, Y, La, Ce, Pr, Nd, Sm, Eu, Tb, Dy, Ho, Er, Tm, Yb, and Lu), Th and U.

Gelatine standards were prepared from porcine gelatine (Sigma-Aldrich, Germany). 1 g of gelatine was mixed with 9 g of ultrapure water and shaken vigorously and heated to approx. 60 °C to 70 °C. After complete dissolution, element standards (Mg, Cr, Mn, Ni, Co, Cu, Zn, Ga, Sr, Ag, Ce, Pr, Tm, Tl, Bi, and Pb) were added to yield a final nominal concentration of 250 μg g⁻¹ for each analyte. The mixture was homogenized and 10 μL droplets were placed on a microscope slide manually using an air displacement pipette (Eppendorf, Germany) and dried overnight at 100 °C before use.

Gelatine standards were digested by weighing 30 mg of each sample (6 replicates) and adding 0.5 mL sub-boiled HNO₃, 0.15 mL H₂O₂ (35%, Acros Organics, Netherlands) and 0.15 mL ultrapure water. All samples were digested using a turboWAVE microwave assisted digestion system (MLS GmBH, Germany). Following digestion, vessels were rinsed three times with 3 mL of ultrapure water each and the digests were diluted to a final volume of 45 mL. Elemental analysis was carried out by SN-ICP-OES. The temperature ramp and maximum power settings for the digestion are provided in Fig. S38 and Table S1.†

Matrix influence

Matrix influence was first investigated using mixtures of HNO₃/HCl at varying concentrations (0.5%/0.5%, 1%/1%, 2%/1%, 1%/2%, and 2%/2%). Further studies on matrix effects focused on selected matrix elements added individually into a multi-element solution (0.05 μg g⁻¹ analytes) stabilized in 1% sub-boiled HNO₃. Equimolar fractions of Al (0–10 μg g⁻¹), Si (0–10 μg g⁻¹), Ca (0–15 μg g⁻¹), Ti (0–18 μg g⁻¹) or Fe (0–20 μg g⁻¹) were added individually to identical multi-element solutions. To investigate the combined effect of all selected matrix elements, solutions containing 3.7 nmol g⁻¹ to 370 nmol g⁻¹ of each element (Al, Si, Ca, Ti and Fe) were added to a multi element solution (0.05 μg g⁻¹ analytes). Droplets were generated at a 50 Hz dispensing rate and measured at a time resolution of 3 ms for a total duration of 1.5 min. The resulting signals were

This journal is © The Royal Society of Chemistry 2025

J. Anal. At. Spectrom., 2025, **40**, 2438–2446 | **2439**

averaged over all droplets to obtain mean intensities from which sensitivities were calculated.

To compare droplet-based results with conventional sample introduction, all Al-containing solutions were also analyzed using solution nebulization ICP-MS (SN-ICP-MS). Measurements were carried out using a dual sample introduction setup[25] connected to a cyclonic double-pass spay chamber equipped with a microflow nebulizer. Data were acquired at a time resolution of 92 ms for a total of 60 s per condition.

Radial diffusion profiles

Measurements were performed at a sampling depth of 3.5 mm, which represented the shortest achievable position under the given instrumental conditions. This was done to minimize sensitivity losses from radial diffusion and to replicate typical quantification conditions. To ensure consistency, radial diffusion profiles were always recorded in the same horizontal direction (right to left). For each profile (microdroplets and laser aerosol), the scanning range was defined by first locating the position of the maximum signal intensity of the $^{238}U^+$ signal and moving laterally across the plasma until signal intensity decreased to 10% of its maximum value. From this position, data were acquired in horizontal steps of 0.3 mm until the maximum signal was reached. Beyond the maximum, the step size was reduced to 0.15 mm and data acquisition continued until a 99% signal decrease was observed or the instrument limit was reached. Diffusion profiles were recorded at 3 ms time resolution for dry laser ablation of NIST SRM 610 (glass, 44 μm spot size, 5 × 5 raster, 7 shots per spot, 10 Hz) and for microdroplets containing a nominal analyte concentration of 0.05 μg g^{-1} and Si concentration of 20 μg g^{-1} dispensed at a frequency of 50 Hz.

Quantification of laser-induced aerosols

Proof of principle and optimization studies were conducted using NIST SRM 610 (glass). Preferred literature values for all CRMs were obtained from the GeoRem database.[36] Laser ablation sampling was performed as a 10 × 10 raster with 7 shots per spot at a 10 Hz repetition rate using a 44 μm spot size at a time resolution of 3 ms. This yielded 100 individual signal peaks, which were integrated for quantification. Droplet data were acquired at a dispensing rate of 50 Hz and processed in the same data structure. Signals from approx. 6000 droplets were integrated and averaged before being used to quantify LA intensities. Quantification was performed using microdroplets containing 0.25 μg g^{-1} of Mg, Cr, Mn, Co, Ni, Cu, Zn, Ga, Sr, Ag, Tl, Pb, and Bi, and 0.05 μg g^{-1} of Sc, Rh, Y, La, Ce, Pr, Nd, Sm, Eu, Gd, Tb, Dy, Ho, Er, Tm, Yb, Lu, Re, Pt, Au, Th and U. For all measurements, Sr was used as the internal standard. To evaluate applicability of the method, CRMs and in-house samples with varying matrix compositions were analyzed, including NIST SRM 612 (glass), USGS BCR-2G (basalt glass), USGS MACS-3 (carbonate) and in-house prepared gelatine standards. Quantification was performed for the following analytes: Mg, Cr, Mn, Co, Ni, Cu, Zn, Rh, Ag, REEs, Re, Pt, Au, Tl, Pb, Bi, Th and U. To compare the performance of the microdroplet-based quantification with conventional approaches, all samples were quantified using NIST SRM 610 (glass) and the droplet-based calibrant as external standards. Quantification was carried out according to Longerich[37] (eqn (2)), using relative sensitivity factors (RSFs). The basic assumption is that the RSF determined using microdroplets equals the RSF of the laser-induced aerosol,

$$RSF_{droplet} = RSF_{laser\ aerosol} \tag{1}$$

which can be expressed as:

$$\left(\frac{\frac{I_A}{I_{IS}}}{\frac{c_A}{c_{IS}}}\right)_{droplet} = \left(\frac{\frac{I_A}{I_{IS}}}{\frac{c_A}{c_{IS}}}\right)_{laser\ aerosol} \tag{2}$$

Data processing

Data from both laser ablation and droplet measurements were processed using in-house write R scripts within the RStudio environment[38,39] (RStudio version 2024.12.1) and Microsoft Excel (Microsoft 365). Peak integration, averaging, and background correction were performed prior to quantification. Relative sensitivity factors (RSFs) were calculated based on the approach described by Longerich et al.[37] Data visualization was carried out using OriginPro 2024 (OriginLab, USA).

Results & discussion

Matrix influence

The influence of Al on analyte sensitivity is depicted as relative signal suppression in Fig. 1 and 2 corresponding to sampling depths of 3 mm and 9 mm, respectively. Additional data on signal suppression of other matrix elements (Fig. S1 to S9†), sensitivity curves (Fig. S10 to S19†), $^{232}Th^{16}O^+/^{232}Th^+$ formation rate and $^{238}U^+/^{232}Th^+$ ratios (Fig. S20 to S23†) are provided in the ESI.†

At a sampling depth of 3 mm, Al exerts a pronounced effect on the sensitivity of the rare earth elements (REEs) and Th, while elements such as Sr, Rh, In and U exhibit minimal to no signal suppression upon Al addition. Elements such as Ce, Eu and Yb display sensitivity spikes, whereas Y and Lu show the strongest observed signal suppression. Although Ce, Eu and Yb are part of redox pairs, similar trends are not observed for Sm and Tb.

No apparent correlation was observed between signal suppression or spike behavior and physicochemical properties such as the ionization potential (IP), melting point (T_m), boiling point (T_b), heat capacity (c_P) or magnetic susceptibility (χ). A minor mass bias in signal suppression is visible, with decreased suppression for the lighter REEs, with the exception of Y. Based on these findings, we propose three hypotheses to explain the observed selective signal suppression:

(i) Chemical reactions during droplet transport or within the ICP, such as matrix-analyte cluster formation, result in selective signal suppression.
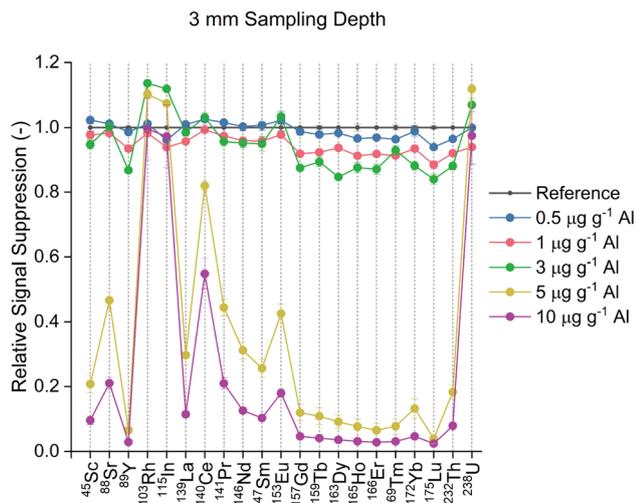
2440 | J. Anal. At. Spectrom., 2025, **40**, 2438–2446

This journal is © The Royal Society of Chemistry 2025

Fig. 1 : Relative signal suppression at 3 mm sampling depth of analytes for no added Al (black), and 0.5 µg g⁻¹ (blue), 1 µg g⁻¹ (red), 3 µg g⁻¹ (green), 5 µg g⁻¹ (yellow) and 10 µg g⁻¹ (purple) of Al.

Fig. 3 Relative signal suppression at 3 mm sampling depth of analytes for no added matrix element (black), 5 µg g⁻¹ of Al (blue), 5 µg g⁻¹ of Si (red), 7.5 µg g⁻¹ of Ca (green), 9 µg g⁻¹ of Ti (yellow) and 10 µg g⁻¹ (purple) of Fe.

(ii) Oxide formation in the plasma caused by thermal pinching due to mass load of either matrix elements or water (l).

(iii) Delayed atomization due to mass load effects as already described by Murtazin *et al.*[40]

Cluster formation can be excluded as the main mechanism. Despite the observed strong signal suppression for elements Y and Lu, no increase in signal intensity was detected at $m/z = 116$ and $m/z = 202$, which would correspond to $^{89}Y^{27}Al^+$ and $^{175}Lu^{27}Al^+$, respectively. Additionally, if cluster formation did play a significant role, a sensitivity spike should have been detected for ^{166}Er due to the potential formation of $^{139}La^{27}Al^+$, which was not the case. However, other chemical reactions in the droplet or formation of a refractory crystalline phase cannot be excluded.
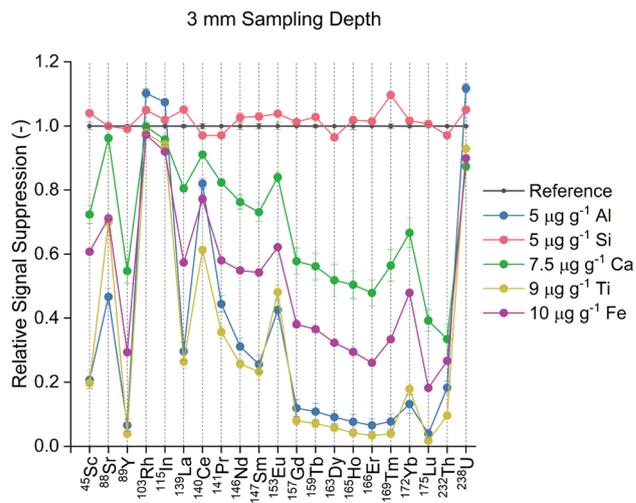
Fig. 3 and 4 illustrate relative signal suppression at single-element equimolar concentrations (*ca.* 0.2 µmol g⁻¹) for Al, Si, Ca, Ti and Fe at 3 mm and 9 mm sampling depths. Despite similar molar fractions, the extent of signal suppression varies between elements. As shown in Fig. 3, Al and Ti induce the strongest signal suppression, followed by Fe and Ca. The collective addition of all selected matrix elements led to significantly stronger signal suppression compared to the individual addition of single elements at equimolar concentrations (see Fig. S9†), particularly at low matrix element concentrations. At 0.5 µg g⁻¹ or 18.5 nmol per g Al (blue line, Fig. 1), analyte signals were reduced by 1% on average. In contrast, when 3.7 nmol g⁻¹ of each matrix element was added

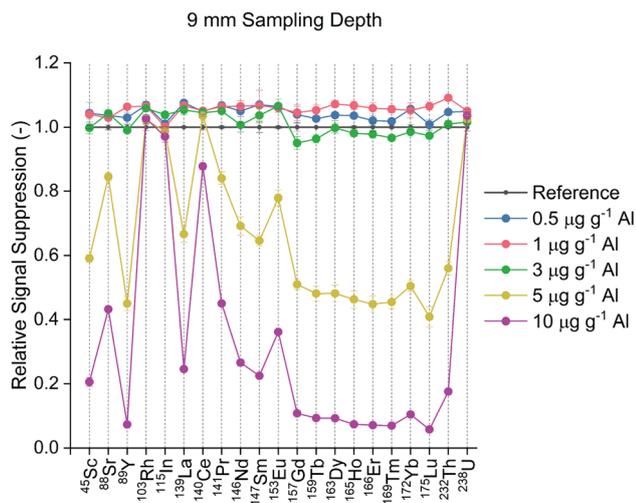**Fig. 2** Relative signal suppression at 9 mm sampling depth of analytes for no added Al (black), and 0.5 µg g⁻¹ (blue), 1 µg g⁻¹ (red), 3 µg g⁻¹ (green), 5 µg g⁻¹ (yellow) and 10 µg g⁻¹ (purple) of Al.

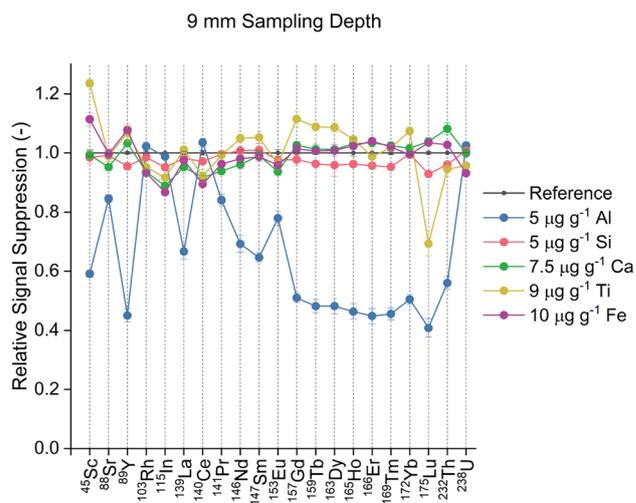**Fig. 4** Relative signal suppression at 9 mm sampling depth of analytes for no added matrix element (black), 5 µg g⁻¹ of Al (blue), 5 µg g⁻¹ of Si (red), 7.5 µg g⁻¹ of Ca (green), 9 µg g⁻¹ of Ti (yellow) and 10 µg g⁻¹ (purple) of Fe.

collectively (blue line, Fig. S9†), the analyte signals were reduced by 12% on average. Addition of 3.7 nmol g^{-1} of each matrix element corresponds to the lowest molar concentration used in a single-element concentration series (for example, 0.5 µg g^{-1} or 18.5 nmol g^{-1} for Al). At higher matrix concentrations (*i.e.*, 5 µg g^{-1} and 10 µg g^{-1} Al or 37 nmol g^{-1} and 74 nmol g^{-1} per element), the magnitude of signal suppression was similar for both single-element and collective matrix addition. Mass load effects can be ruled out, as Si addition does not affect analyte sensitivity. In contrast, oxide formation trends for Al, Ca, Ti and Fe show increasing oxide formation rates with increasing mass fraction for both sampling depths, as shown in Fig. S20 and S21.† This increase in oxides indicates higher energy consumption within the ICP, possibly resulting from matrix-induced processes or reactions. Regarding Si, oxide formation rates are unaffected by increasing mass fractions. The $^{238}U^+/^{232}Th^+$ ratios (Fig. S22 and S23†) show increases up to a factor of 13, while $^{232}Th^{16}O^+/^{232}Th^+$ (Fig. S20 and S21†) formation rates increase only by a factor of up to *ca.* 4. This suggests that mere in-plasma oxide formation cannot account for the extent of signal suppression observed.

If additional matrix induced processes or reactions contribute to signal suppression, increased residence time in the plasma should mitigate these suppression effects. In order to put this hypothesis to the test, measurements were repeated at a sampling depth of 9 mm (Fig. 2 and 4). For all affected elements, an increase in residence time significantly reduces or eliminates signal suppression effects at low matrix mass fractions. However, in order to compensate for matrix-induced processes by an increase in sampling depth, sensitivity decreases by a factor of approx. 4.

Hypotheses (ii) and (iii) are expected to affect analyte behavior similarly and should also be mitigated by an increase in plasma residence time. In order to further investigate analyte suppression, Al containing solutions were measured as well *via* SN-ICP-MS, employing either Ar as the nebulizer gas or an Ar/He mixture (Fig. S24 and S25†) to better simulate drying conditions in the falling tube. SN-generated droplets *via* pneumatic nebulization are polydisperse and if hypotheses (ii) and (iii) are applicable, analyte behavior should be equally influenced irrespective of sample introduction. When Al containing solutions were introduced *via* SN, the resulting sensitivity curves overlapped for all Al mass fractions. This indicates that drying behavior is not influenced by Al addition, which would result in an increased mass load of water (l). Based on these reported findings, all of the 3 suggested hypotheses can be ruled out. In addition, signal suppression behavior seems to be connected to the introduction of the solutions as discrete monodisperse microdroplets instead of a polydisperse aerosol.

Radial diffusion

To compare the in-plasma behavior of laser-induced aerosol (NIST SRM 610 (glass)) and microdroplets, radial diffusion profiles were measured under sampling conditions optimized for quantification. If the evaporation, atomization and ionization position within the plasma differs between the solid
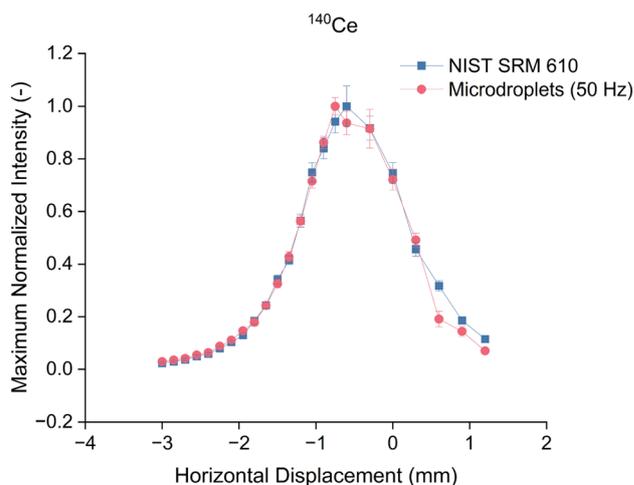

Fig. 5 Radial diffusion intensity distribution of ^{140}Ce for dry ablated NIST SRM 610 (red) and microdroplets (blue) at 50 Hz dispensing frequency.

standard and liquid calibrant, differences in radial diffusion widths are expected: narrower profiles in comparison would indicate delayed evaporation, while broader profiles would suggest earlier evaporation. If the evaporation positions in the plasma are comparable/similar, profiles should overlap and have similar widths based on the full width at half maximum (FWHM).

Radial diffusion profiles are depicted for ^{140}Ce and ^{28}Si in Fig. 5 and 6, representing analytes at vastly different concentrations in NIST SRM 610 (glass), approximately by a factor of 700. To account for evaporation and diffusion differences related to the mass load introduced into the ICP, these two elements were selected due to their differing mass load and *m/z* values. Plotted diffusion profiles for additional mentioned elements are available in the ESI (Fig. S29 to S37†).

For both analytes, the diffusion profiles measured for droplets and laser-induced aerosol largely overlap and exhibit
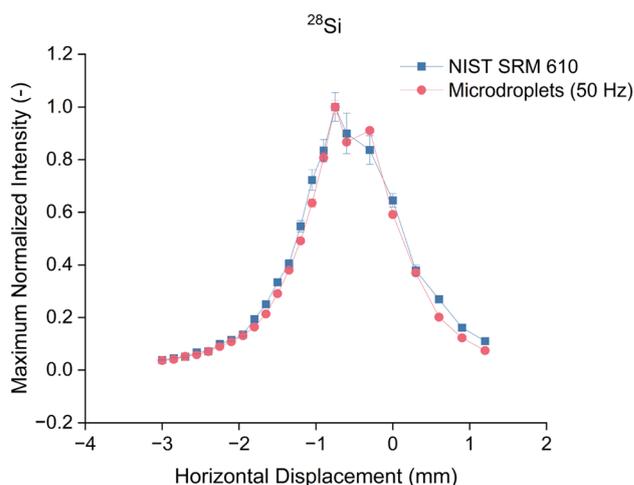

Fig. 6 Radial diffusion intensity distribution of ^{28}Si for dry ablated NIST SRM 610 (red) and microdroplets (blue) at 50 Hz dispensing frequency.
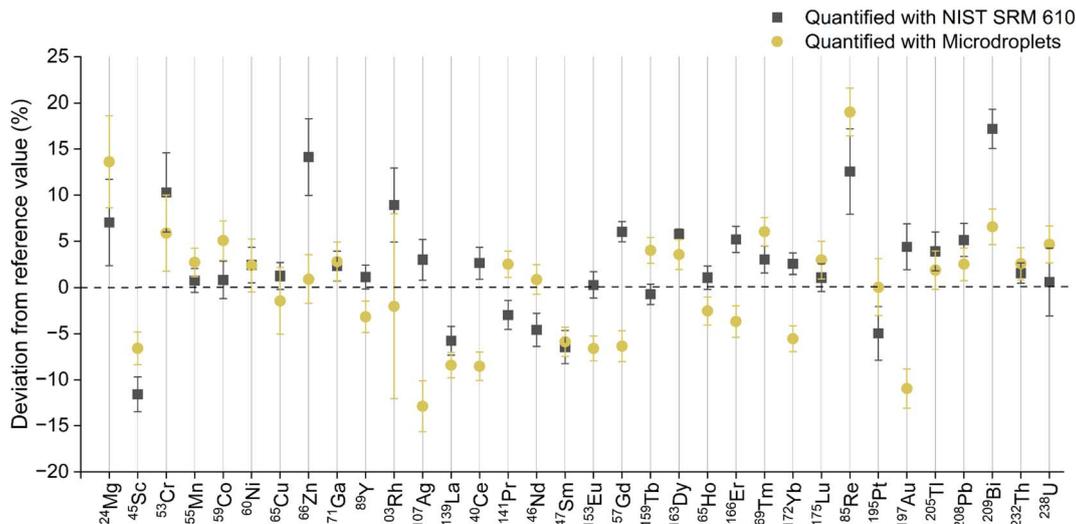
2442 | *J. Anal. At. Spectrom.*, 2025, **40**, 2438–2446

This journal is © The Royal Society of Chemistry 2025

Fig. 7 Deviation from reference values for NIST SRM 612 for quantification using NIST SRM 610 as the external standard (black) and micro-droplets (yellow); microdroplets contained only target analytes (see the Experimental section).

comparable FWHM values and ratios lay between 0.8 and 1.3, as listed in Table S9,† indicating similar evaporation, atomization and ionization positions in the plasma. Slight horizontal offsets in the droplet profiles were observed, likely resulting from a difference in on-axis introduction of the microdroplets, as expected for an injector diameter of 2.5 mm.

While diffusion profiles generally overlap for the measured analytes, those of Y, Gd, Tb, Tm, Dy, Ho, Er, Lu and Th (Fig. S29–S37†) show overlap only across half of the curve, indicating earlier evaporation or an asymmetric ion cloud. The FWHM values of these elements are 30% higher in droplets compared to other analytes, without affecting quantifiability. Despite these shifts in the maximum intensity position and slight asymmetry, the overall similarity in profile shape and width suggests that

droplets and laser-induced aerosol exhibit comparable behavior in the plasma under typical measurement conditions.

Quantification of laser-induced aerosols

Droplet-based quantification was evaluated against NIST SRM 610 (glass) to assess performance across both matrix-matched standards (NIST SRM 612 (glass) and USGS BCR-2G (basalt glass)) and non-matrix-matched standards (USGS MACS-3 (carbonate) and gelatine). The goal was to determine whether droplets can serve as a viable external standard for non-matrix matched quantification in LA-ICP-MS. Relative deviations from the preferred values listed in the GeoRem database[36] are shown in Fig. 7–10.
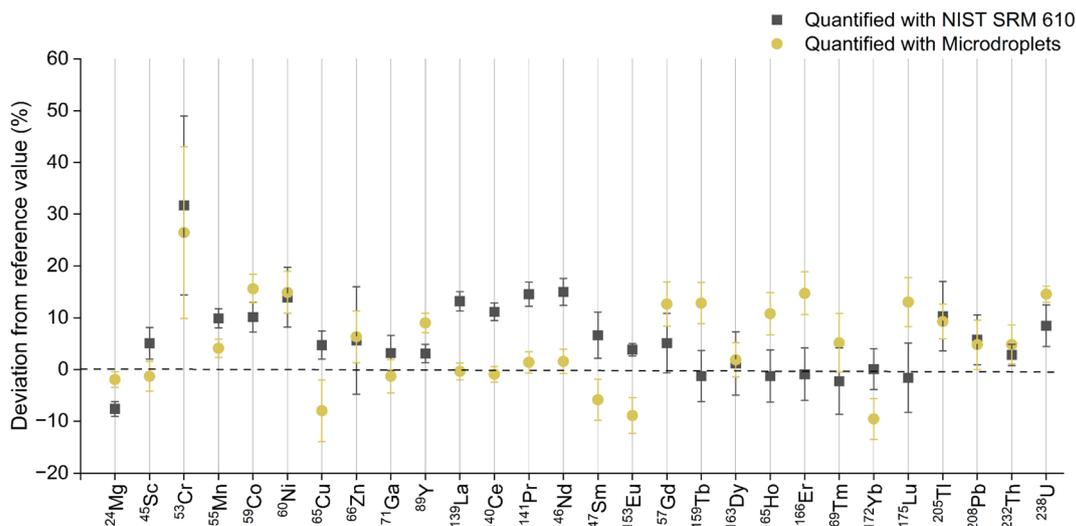

Fig. 8 Deviation from reference values for USGS BCR-2G for quantification using NIST SRM 610 as the external standard (black) and micro-droplets (yellow); microdroplets contained only target analytes (see the Experimental section).
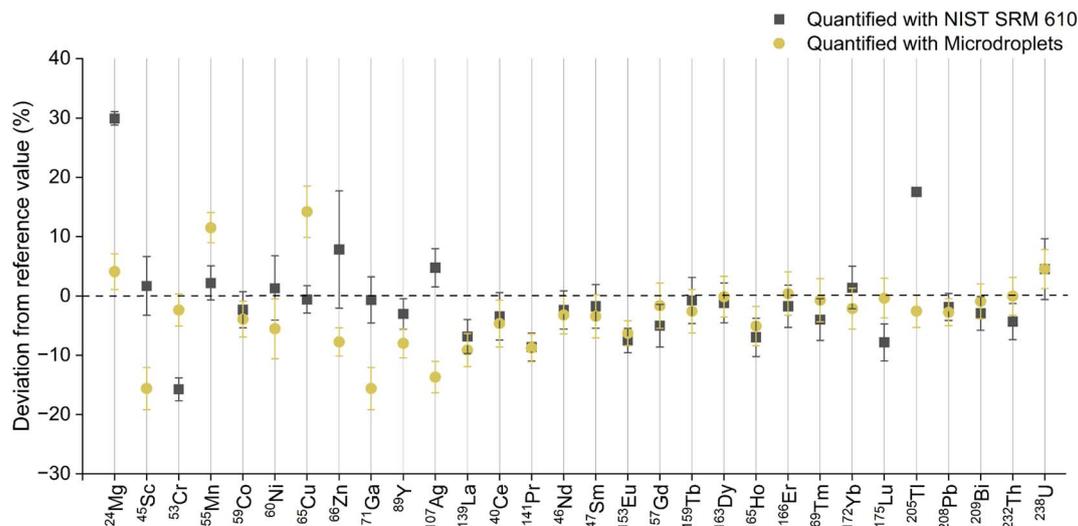
This journal is © The Royal Society of Chemistry 2025

J. Anal. At. Spectrom., 2025, **40**, 2438–2446 | **2443**

Fig. 9 Deviation from reference values for USGS MACS-3 for quantification using NIST SRM 610 as the external standard (black) and microdroplets (yellow); microdroplets contained only target analytes (see the Experimental section).

Across all analyzed matrices, the determined mass fractions were in agreement with literature values, with relative deviations below ±20%. This demonstrates that the microdroplet-based approach is suitable for both inorganic and proteinaceous matrices. However, internal standardization remains essential and total consumption approaches may be limited by differing detection efficiencies between microdroplets and laser-induced aerosols, which was beyond the scope of this study. Accuracy of the microdroplet-based calibration was comparable to NIST SRM 610 (glass) for all inorganic matrices investigated.

When used as an external standard for gelatine quantification, NIST SRM 610 (glass) showed a deviation of ±30%, while microdroplet-based quantification resulted in ±15% of analyzed reference values. This highlights the applicability of

droplets for non-matrix matched quantification when an internal standard can be used.

In all discussed results, ^{88}Sr was used as an internal standard despite being a trace component in the used CRMs and gelatine standard. Ideally, a matrix element should serve as the internal standard, but this was initially avoided due to concerns regarding matrix-induced effects and potential HF traces in element standards, resulting in precipitation of targeted analytes. Since the quantification approach relies on the signal ratio between the analyte and internal standard, and Sr may also be affected by signal suppression from certain matrix constituents, such effects inherently influence the ratio and cannot be fully corrected by internal standardization. As Si showed little to no influence on analyte behavior in earlier experiments, it was evaluated as an internal standard. However,
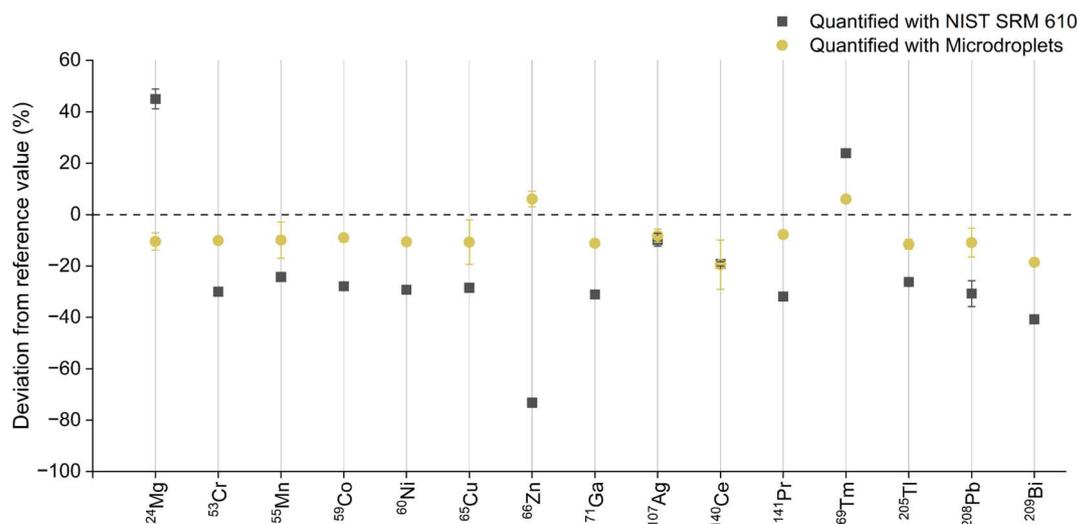

Fig. 10 Deviation from digestion data for in-house prepared gelatine standards for quantification using NIST SRM 610 as the external standard (black) and microdroplets (yellow); microdroplets contained only target analytes (see the Experimental section).

signal-to-noise ratios remained poor due to low sensitivity in the low mass range, high background levels for all Si isotopes and necessary notch-filters, even when high amounts of Si ($20\ \mu g\ g^{-1}$) were added to the calibrant. Consequently, accuracy decreased but was still in good agreement with literature values. The results for Si as the internal standard can be found in the ESI (Fig. S28†).

Conclusion

Influence of matrix-induced effects on microdroplets was investigated and signal suppression behaviors for Al, Si, Ca, Ti and Fe were evaluated. The observed suppression patterns can neither be explained by common effects such as mass load nor oxide formation. To determine whether these patterns are also apparent using other liquid sample introduction techniques, Al containing solutions were introduced *via* solution nebulization. No comparable signal suppression was observed, suggesting a unique behavior of discretely introduced microdroplets in the ICP. To further investigate potential differences in the in-plasma behavior between microdroplets and the laser-induced aerosol, radial diffusion profiles were obtained without addition of matrix elements known to cause signal suppression. Microdroplets and laser-induced aerosol of NIST SRM 610 (glass) exhibit comparable in-plasma behavior based on the radial diffusion profiles. Although horizontal shifts between microdroplets and laser-induced aerosol suggest a difference in on-axis introduction of the droplets, it however, does not affect quantification accuracy. Quantification results of inorganic matrices using droplets show general deviations below $\pm 20\%$ and perform comparable to NIST SRM 610 (glass) when employed as a matrix-matched and non-matrix-matched standard. While quantification of the in-house gelatine standard using NIST SRM 610 (glass) showed deviations $\pm 30\%$, microdroplets yielded values $\pm 15\%$ compared to digestion data. However, an internal standard is required, as detection efficiencies cannot be assumed to be comparable. Despite the general agreement of $\pm 20\%$, possible limitations of the proposed microdroplet-based quantification approach should be considered. First, if laser-induced aerosols contain a significant fraction of large particles, incomplete transport to the plasma, *e.g.*, due to particle loss within the tubing or incomplete vaporization in the plasma can lead to inaccurate quantification. This is particularly relevant for aerosols generated under an argon atmosphere or with longer wavelength lasers, both of which are known to produce broader particle size distributions and contribute to elemental fractionation.[31,41,42] Second, analytes that partially enter the plasma in the gaseous form may lead to biased results, as differences in transport and ionization behavior between gaseous species and the particulate-phase are not accounted for in the current approach. Lastly, quantification may be affected if matrix-induced effects affect the in-plasma behavior of the laser aerosol such that the analyte and the internal standard no longer exhibit similar ionization characteristics compared to the microdroplets. These first two limitations can be mitigated by using short-pulsed, flat-top deep-UV lasers in combination with fast-washout ablation

cells and helium as the carrier gas, which have been shown to reduce particle size,[41,42] improve transport characteristics,[43–45] and minimize elemental fractionation.[31,46,47] This study demonstrates that monodisperse microdroplets can be employed as a non-matrix-matched external standard for quantification of laser-induced aerosols in ICP-TOFMS. Microdroplets can be utilized for the quantitative analysis of a range of matrices, including inorganic and proteinaceous samples and offer great flexibility in analytes and concentration ranges.

Data availability

The data supporting this article have been included as part of the ESI.†

Author contributions

Conflicts of interest

There are no conflicts of interest to declare.

Acknowledgements

References

1 A. L. Gray, *Analyst*, 1985, **110**, 551–556.
2 T. Van Acker, S. Theiner, E. Bolea-Fernandez, F. Vanhaecke and G. Koellensperger, *Nat. Rev. Methods Primers*, 2023, **3**, 52.
3 B. J. Fryer, S. E. Jackson and H. P. Longerich, *Can. Mineral.*, 1995, **33**, 303–312.
4 J. S. Becker, M. V. Zoriy, C. Pickhardt, N. Palomero-Gallagher and K. Zilles, *Anal. Chem.*, 2005, **77**, 3208–3216.
5 S. E. Jackson, in *Laser Ablation ICP-MS in the Earth Sciences: Current Practices and Outstanding Issues*, 2008, vol. 40, pp. 169–188.
6 A. Schweikert, S. Theiner, D. Wernitznig, A. Schoeberl, M. Schaier, S. Neumayer, B. K. Keppler and G. Koellensperger, *Anal. Bioanal. Chem.*, 2022, **414**, 485–495.
7 M. Šala, V. S. Šelih and J. T. Van Elteren, *Analyst*, 2017, **142**, 3356–3359.

This journal is © The Royal Society of Chemistry 2025

J. Anal. At. Spectrom., 2025, **40**, 2438–2446 | **2445**

8 M. Thompson, S. Chenery and L. Brett, *J. Anal. At. Spectrom.*, 1989, **4**, 11–16.

9 E. F. Cromwell and P. Arrowsmith, *Anal. Chem.*, 1995, **67**, 131–138.

10 D. Günther, R. Frischknecht, H.-J. Müschenborn and C. A. Heinrich, *Fresenius. J. Anal. Chem.*, 1997, **359**, 390–393.

11 D. Günther, H. Cousin, B. Magyar and I. Leopold, *J. Anal. At. Spectrom.*, 1997, **12**, 165–170.

12 L. Halicz and D. Günther, *J. Anal. At. Spectrom.*, 2004, **19**, 1539–1545.

13 P. W. J. M. Boumans and F. J. De Boer, *Spectrochim. Acta, Part B*, 1976, **31B**, 355–375.

14 E. T. Luong, R. S. Houka and R. E. Serfass, *J. Anal. At. Spectrom.*, 1997, **12**, 703–708.

15 M. Kuonen, B. Hattendorf and D. Günther, *J. Anal. At. Spectrom.*, 2024, **39**, 1388–1397.

16 L. Yang, R. E. Sturgeon and Z. Mester, *J. Anal. At. Spectrom.*, 2005, **20**, 431–435.

17 W. Nischkauer, F. Vanhaecke and A. Limbeck, *Anal. Bioanal. Chem.*, 2016, **408**, 5671–5676.

18 D. N. Douglas, J. L. Crisp, H. J. Reid and B. L. Sharp, *J. Anal. At. Spectrom.*, 2011, **26**, 1294–1301.

19 C. Herzig, J. Frank, A. K. Opitz, J. Fleig and A. Limbeck, *Talanta*, 2020, **217**, 1–7.

20 K. Mervič, J. T. van Elteren, M. Bele and M. Šala, *Talanta*, 2024, **269**, 125379.

21 K. Mervič, V. S. Šelih, M. Šala and J. T. van Elteren, *Talanta*, 2024, **271**, 125712.

22 G. M. Hieftje and H. V. Malmstadt, *Anal. Chem.*, 1968, **40**, 1860–1867.

23 J. W. Olesik, *Appl. Spectrosc.*, 1997, **51**, 158A–175A.

24 S. Gschwind, L. Flamigni, J. Koch, O. Borovinskaya, S. Groh, K. Niemax and D. Günther, *J. Anal. At. Spectrom.*, 2011, **26**, 1166–1174.

25 B. Ramkorun-Schmidt, S. A. Pergantis, D. Esteban-Fernández, N. Jakubowski and D. Günther, *Anal. Chem.*, 2015, **87**, 8687–8693.

26 L. Hendriks, B. Ramkorun-Schmidt, A. Gundlach-Graham, J. Koch, R. N. Grass, N. Jakubowski and D. Günther, *J. Anal. At. Spectrom.*, 2019, **34**, 716–728.

27 A. Gundlach-Graham and K. Mehrabi, *J. Anal. At. Spectrom.*, 2020, **35**, 1727–1739.

28 C. C. Garcia, A. Murtazin, S. Groh, M. Becker and K. Niemax, *Spectrochim. Acta, Part B*, 2010, **65**, 80–85.

29 C. C. Garcia, A. Murtazin, S. Groh, V. Horvatic and K. Niemax, *J. Anal. At. Spectrom.*, 2010, **25**, 645–653.

30 J. Koch, L. Flamigni, S. Gschwind, S. Allner, H. Longerich and D. Günther, *J. Anal. At. Spectrom.*, 2013, **28**, 1707–1717.

31 H. R. Kuhn, M. Guillong and D. Günther, *Anal. Bioanal. Chem.*, 2004, **378**, 1069–1074.

32 O. Borovinskaya, PhD thesis, ETH Zurich, 2014.

33 P. Becker and D. Günther, *J. Anal. At. Spectrom.*, 2023, **38**, 1704–1712.

34 M. Burger, G. Schwarz, A. Gundlach-Graham, D. Käser, B. Hattendorf and D. Günther, *J. Anal. At. Spectrom.*, 2017, **32**, 1946–1959.

35 J. M. Mermet, *Spectrochim. Acta, Part B*, 1989, **44B**, 1109–1989.

36 K. P. Jochum, U. Nohl, K. Herwig, E. Lammel, B. Stoll and A. W. Hofmann, *Geostand. Geoanal. Res.*, 2005, **29**, 333–338.

37 H. P. Longerich, S. E. Jackson and D. Günther, *J. Anal. At. Spectrom.*, 1996, **11**, 899–904.

38 R Core Team, *R Foundation for Statistical Computing*, R Foundation for Statistical Computing, Vienna, 2021.

39 RStudio, *RStudio*, PBC, Boston MA, 2025.

40 A. Murtazin, S. Groh and K. Niemax, *Spectrochim. Acta, Part B*, 2012, **67**, 3–16.

41 I. Horn and D. Günther, *Appl. Surf. Sci.*, 2003, **207**, 144–157.

42 M. Guillong, I. Horn and D. Günther, *J. Anal. At. Spectrom.*, 2003, **18**, 1224–1230.

43 E. L. Gurevich and R. Hergenröder, *J. Anal. At. Spectrom.*, 2007, **22**, 1043–1050.

44 M. B. Fricker, D. Kutscher, B. Aeschlimann, J. Frommer, R. Dietiker, J. Bettmer and D. Günther, *Int. J. Mass Spectrom.*, 2011, **307**, 39–45.

45 C. Neff, P. Becker and D. Günther, *J. Anal. At. Spectrom.*, 2022, **37**, 677–683.

46 M. Guillong and D. Günther, *J. Anal. At. Spectrom.*, 2002, **17**, 831–837.

47 P. Becker, J. Koch and D. Günther, *J. Anal. At. Spectrom.*, 2022, **37**, 1846–1854.

2446 | *J. Anal. At. Spectrom.*, 2025, **40**, 2438–2446

This journal is © The Royal Society of Chemistry 2025